Hierarchically structured diamond composite with exceptional toughness

https://doi.org/10.1038/s41586-020-2361-2

Received: 16 August 2019

Accepted: 23 March 2020

Published online: 17 June 2020

Check for updates

Yonghai Yue[1,2,7], Yufei Gao[1,7], Wentao Hu[1,7], Bo Xu[1,7], Jing Wang[2], Xuejiao Zhang[2], Qi Zhang[2], Yanbin Wang[3], Binghui Ge[4], Zhenyu Yang[5], Zihe Li[1], Pan Ying[1], Xiaoxiao Liu[1], Dongli Yu[1], Bin Wei[6], Zhongchang Wang[6], Xiang-Feng Zhou[1]✉, Lin Guo[2]✉ & Yongjun Tian[1]✉

The well known trade-off between hardness and toughness (resistance to fracture) makes simultaneous improvement of both properties challenging, especially in diamond. The hardness of diamond can be increased through nanostructuring strategies[1,2], among which the formation of high-density nanoscale twins — crystalline regions related by symmetry — also toughens diamond[2]. In materials other than diamond, there are several other promising approaches to enhancing toughness in addition to nanotwinning[3], such as bio-inspired laminated composite toughening[4–7], transformation toughening[8] and dual-phase toughening[9], but there has been little research into such approaches in diamond. Here we report the structural characterization of a diamond composite hierarchically assembled with coherently interfaced diamond polytypes (different stacking sequences), interwoven nanotwins and interlocked nanograins. The architecture of the composite enhances toughness more than nanotwinning alone, without sacrificing hardness. Single-edge notched beam tests yield a toughness up to five times that of synthetic diamond[10], even greater than that of magnesium alloys. When fracture occurs, a crack propagates through diamond nanotwins of the 3C (cubic) polytype along {111} planes, via a zigzag path. As the crack encounters regions of non-3C polytypes, its propagation is diffused into sinuous fractures, with local transformation into 3C diamond near the fracture surfaces. Both processes dissipate strain energy, thereby enhancing toughness. This work could prove useful in making superhard materials and engineering ceramics. By using structural architecture with synergetic effects of hardening and toughening, the trade-off between hardness and toughness may eventually be surmounted.

Diamond is essential for a wide range of industrial and scientific applications. Although its hardness is unparalleled, its toughness is inferior to that of many known tool materials[11]. Increasing its hardness still further (for instance to offer better machining efficiency and precision, or higher achievable pressure ranges in diamond anvil cells) usually results in lower toughness, shortening the lifetime of diamond tools. Improving toughness and hardness simultaneously is challenging because of the intrinsic brittleness of diamond. Fortunately, studies on various materials provide valuable clues for toughening mechanisms in diamond. Twin boundaries (TBs) are superior to large-angle grain boundaries in optimizing the mechanical properties of both diamond and metals[2,12–14]. Nanotwinned diamond (nt-diamond) exhibits tremendous hardness enhancement without sacrificing fracture toughness[2]. A nanotwin-governed toughening mechanism also occurs in conch shells with high-density nanotwins[3]. Ceramic-based composites with brick-and-mortar structures similar to those of natural nacre demonstrate another way to improve material toughness[4–7]: the microstructure has alternating layers of constituents whose interacting interfaces have fundamental roles. Transformation toughening occurs in, for example, partially stabilized zirconia, where a tetragonal to monoclinic transformation occurs[8]; similarly, as there are numerous diamond polytypes with various stacking sequences of carbon bilayers[15], a transformation between diamond polytypes might also contribute to toughening.

During synthesis of nt-diamond bulk materials, we noticed that the final products from carbon onion precursors depended on synthesis pressure[2]. Products synthesized at 18–25 GPa were pure nt-diamond, whereas those at pressures below 18 GPa were composites consisting of diamond nanotwin domains and thin slices of metastable carbon phases (denoted M-diamond at the time[2]) epitaxially confined within diamond nanotwins. We systematically investigated the microstructure and mechanical properties of these nt-diamond composites. Transmission electron microscopy (TEM) characterizations confirm that the main phase is nt-diamond (3C polytype; Fig. 1). With advances in

[1]Center for High Pressure Science, State Key Laboratory of Metastable Materials Science and Technology, Yanshan University, Qinhuangdao, China. [2]School of Chemistry, Beijing Advanced Innovation Center for Biomedical Engineering, Beihang University, Beijing, China. [3]Center for Advanced Radiation Sources, University of Chicago, Chicago, IL, USA. [4]Institute of Physical Science and Information Technology, Anhui University, Hefei, China. [5]Institute of Solid Mechanics, School of Aeronautics Sciences and Engineering, Beihang University, Beijing, China. [6]Department of Quantum and Energy Materials, International Iberian Nanotechnology Laboratory, Braga, Portugal. [7]These authors contributed equally: Yonghai Yue, Yufei Gao, Wentao Hu, Bo Xu. ✉e-mail: xfzhou@nankai.edu.cn; guolin@buaa.edu.cn; fhcl@ysu.edu.cn

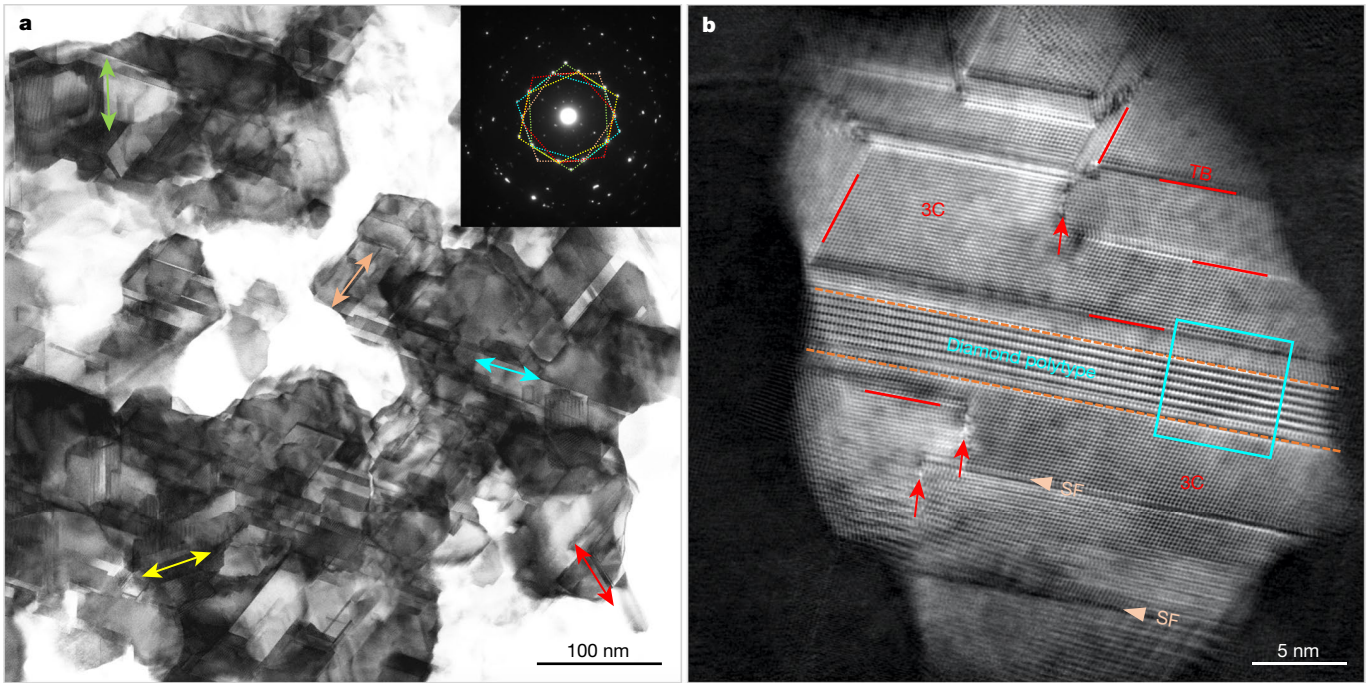

Fig. 1 | Typical microstructure of nt-diamond composite synthesized at 15 GPa and 2,000 °C. a, A low-magnification bright-field STEM image showing interlocked grains constituted of nanotwins. The coloured double-arrows indicate different TB orientations. Inset shows the corresponding selected-area electron diffraction pattern with an apparent fivefold symmetry due to multiple twinning in the interlocked grains. **b**, A high-magnification ADF-STEM image of a grain with nanotwins and coherently embedded diamond polytype domains. {111} TBs (red lines), intrinsic stacking faults (SF; arrowheads) and lateral Σ3(211) TBs (red arrows) are marked.

sample preparation and characterization techniques (see Methods), we now have sufficient evidence that 'M-diamond' is in fact a range of non-3C polytypes (such as 2H, 4H, 9R or 15R) embedded in 3C nanotwins (Fig. 2). Single-edge notched beam (SENB) tests of nt-diamond composite reveal an exceptional toughness as high as 26.6 MPa $m^{1/2}$, five times that of synthetic diamond[10]. Further in situ fracture testing in TEM reveals two modes of crack propagation. Within 3C nanotwins, the crack propagates along {111} planes and changes direction abruptly at TBs, forming a zigzag path. When entering regions of non-3C polytypes, the crack propagation path becomes sinuous and wavy, accompanied by local transformation from non-3C polytypes to the 3C one.

We synthesized nt-diamond composite from onion carbons (see Methods). TEM foils were prepared by focused ion-beam (FIB) milling as described in the Methods. Figure 1 shows the typical microstructure of the composite. The bright-field scanning TEM (STEM) image (Fig. 1a) indicates tightly bound nanograins composed of numerous nanotwins. The corresponding selected-area electron diffraction pattern (inset in Fig. 1a) displays an apparent fivefold symmetry originating from the multiply twinned structures of interlocked nanograins, which are further confirmed in Extended Data Figs. 1 and 2. The high-magnification annular dark-field (ADF) STEM image (Fig. 1b) shows details of a nanograin, in which nanotwins, stacking faults (SFs) and secondary phases similar to the previously observed M-diamond are clearly revealed. 3C diamond nanotwins with thicknesses of several nanometres and various orientations are interwoven with {111} TBs. Sometimes, the {111} TBs are offset by step-like features (red arrows, Fig. 1b), which are low-energy Σ3(211) TBs other than the conventional {111} ones and may act as dislocation sources during deformation[13,16,17].

Our results show that 'M-diamond' is actually several non-3C diamond polytypes that interface coherently with each other and with 3C diamond. Figure 2 shows representative atomic-resolution high-angle annular dark-field (HAADF) STEM images of such polytypes, taken along the [10$\bar{1}$] zone axis of 3C diamond. Nanotwins are pervasive in regions dominated by 3C diamond, in which close-packed carbon bilayers are stacked with a sequence of ABC (Fig. 2a). The inset summarizes the twinning relations between labelled nanotwins that share common {111} planes. Other types of TBs (such as Σ9 TBs) and localized atomic rearrangements operate together to lock neighbouring nanotwins that do not share common {111} planes, as indicated by the yellow dashed line and ovals, respectively, in Fig. 2a. Thin slices of 2H and 4H polytypes, with stacking sequences AB and ABAC, respectively, are coherently sandwiched between 3C nanotwins.

Polytypes as such are not rare in our STEM observations. On the contrary, abundant non-3C polytypes coexist with 3C diamond (Fig. 2, Extended Data Fig. 2), justifying the term 'nt-diamond composite'. Figure 2b shows a HAADF-STEM image corresponding to the cyan box in Fig. 1b. A slice of 2H polytype, about 3 nm in thickness and tens of nanometres in width, is identified between two 3C domains. The fast Fourier transformation (FFT) pattern (inset) confirms the symmetry of 2H diamond. The superposed atomic packing model of 2H polytype shows a perfect match with the HAADF observation (Fig. 2b). This 2H slice forms coherent interfaces with the neighbouring 3C domains, with the epitaxial relation $(111)_{3C}//(0001)_{2H}$. Such coherent interfaces are characteristics of all polytypes identified in the composite. Slices of other polytypes, such as 9R and 15R, are also identified from HAADF measurements, as shown in Fig. 2c with the atomic models superposed. The FFT pattern corresponding to Fig. 2c (inset) indicates a tripling of the periodicity for $(111)_{3C}$ that can be attributed to the epitaxy of diamond polytypes, such as $(111)_{3C}//(009)_{9R}$. It is the stacking sequence of carbon bilayers that differentiates one polytype from another. Extended Data Fig. 2f–h shows stacking sequences of carbon bilayers for selected polytypes and simulated electron diffraction patterns of 2H, 9R and 15R, all in excellent agreement with experimental FFT patterns (insets in Fig. 2b and c). Localized layer-defects are routinely observed, with interlayer distance substantially larger than that of typical carbon bilayers (dashed ellipses in Fig. 2c) and substantial sp^2 bonding (Extended Data Fig. 3).

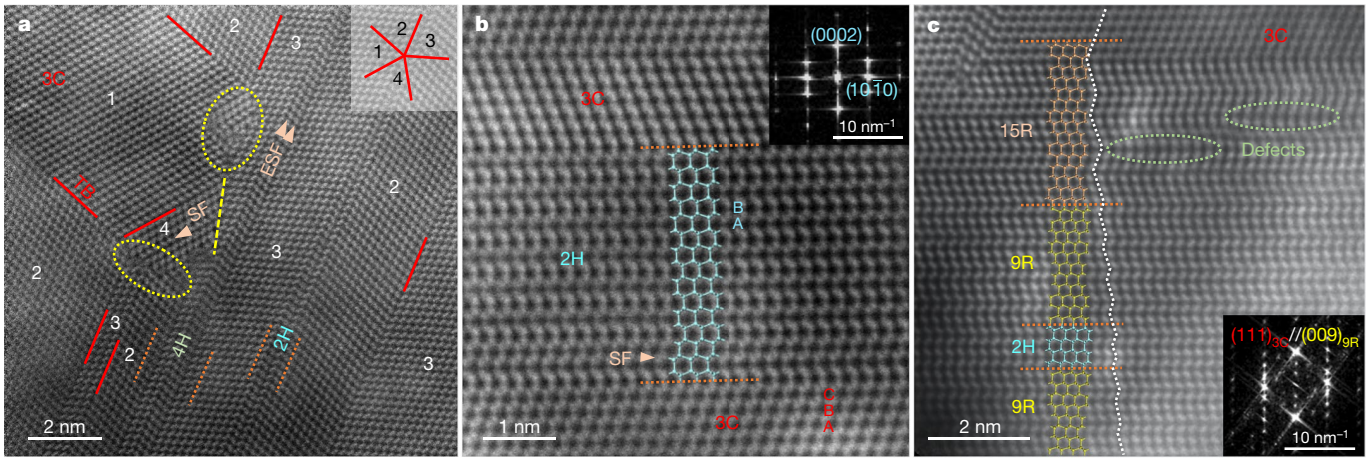

Fig. 2 | HAADF-STEM images of nt-diamond composite synthesized at 15 GPa and 2,000 °C. a, An nt-diamond-dominated region where TBs (red lines), stacking fault (arrowhead), extrinsic SF (ESF; double-arrowhead), 2H and 4H diamond polytypes are marked. Within each twin domain, the structure is 3C. Inset shows twinning relations between labelled nanotwin domains, with TBs indicated by red lines. **b**, A high-resolution HAADF-STEM image from the cyan-boxed region in Fig. 1b, containing 3C diamond (top and bottom) and a slice of coherently embedded 2H polytype (middle). Inset is the corresponding FFT pattern of the 2H region, showing symmetry different from that of 3C diamond. A stacking fault in 2H-diamond is indicated. **c**, A high-resolution HAADF-STEM image of nanotwinned diamond with coherently embedded 2H, 9R and 15R polytypes. Inset is the corresponding FFT pattern, showing a tripling of the $(111)_{3C}$ periodicity. In the 15R region, two localized layer-defects are indicated by the dashed ovals.

Our HAADF-STEM observations provide electron microscopic evidence of diamond polytypes that have long been debated[18,19]. The *d*-spacings (the distance between planes of atoms that give rise to the diffraction peaks) determined from FFT of HAADF-STEM images of nt-diamond composite are listed in Extended Data Table 1. All the observed *d*-spacings that do not belong to 3C diamond can be attributed to non-3C polytypes, further confirming the coexistence of diamond polytypes in our composite. During high-pressure synthesis, the sp^2-bonded carbon atoms in onion-structured precursors pucker into carbon bilayers and link into sp^3-bonded carbon, with C–C bonds forming between neighbouring bilayers. Pressure is essential in controlling the formation of polytypes. At high pressures such as 20 GPa, the stacking sequence of carbon bilayers is exclusively of 3C type, and pure nt-diamond is produced[2]. At relatively low pressures (<18 GPa), a series of non-3C polytypes with stacking sequences other than 3C type are formed, yielding a composite rich in polytypes. Complex pressure drops at various time and length scales may occur in the sample owing to the greatly reduced specific volume during phase transformation, as has been observed in situ in forsterite[20]. We speculate that, owing to transformation-induced pressure heterogeneities, some sp^2-bonded carbon layers may not have experienced sufficient driving force to adjust into the most stable 3C structure within the synthesis time frame of our experiments. Such a process is similar to what occurs in sheared highly disordered nanocrystalline hexagonal boron nitride[21], in which wurtzite-type BN analogous to 2H diamond forms even at room temperature. On the other hand, the more stable cubic BN, analogous to 3C diamond, forms only under high pressure and temperature.

The Vickers hardness of nt-diamond composite measured with a load of 4.9 N is 200.1 ± 8.0 GPa, similar to that of nt-diamond[2]. On the other hand, nt-diamond composite possesses a hierarchical microstructure more complex than that of nt-diamond. In this composite, non-3C diamond polytypes are coherently embedded in 3C nanotwins (several nanometres in thickness) interwoven into mosaic-structured nanograins (tens of nanometres in size). The nanograins are tightly interlocked with a high percentage of low-energy boundaries (Extended Data Fig. 4). The hierarchical structure has an essential role in toughening the composite. Fracture toughness of this hierarchically structured composite was determined with standard SENB tests in a scanning electron microscope (SEM)[4,5,22]. Test beams bridging the excavated 'craters' were prepared with FIB milling (Extended Data Fig. 5a–c). Figure 3a–d shows chronologically ordered images of sample 3 during the test. A crack initiated at the tip of the precut notch, propagated first to the upper right (Fig. 3b), then turned almost 90° and extended to the upper left (Fig. 3c). The large-angle crack deflection, which consumes additional energy[3,5], suggests exceptional fracture toughness of the nt-diamond composite.

Force–displacement curves from the multi-cycle load–unload bending test are shown in Extended Data Fig. 5j, revealing an exceptionally high fracture toughness of 26.6 MPa m$^{1/2}$, five times the reported values of synthetic diamond[10]. The toughness values from our SENB tests for a series of samples of nt-diamond composite, pure nt-diamond (synthesized at 20 GPa and 2,000 °C) and commercial yttria partially stabilized zirconia (Y-PSZ, Beilong Electronics, China) are listed in Extended Data Table 2. The toughness of Y-PSZ (8.1 ± 1.2 MPa m$^{1/2}$) is consistent with the value of 8–11 MPa m$^{1/2}$ provided by the manufacturer. We also measured Vickers indentation fracture toughness (Extended Data Fig. 6). Although the indentation toughness values are systemically lower than the SENB ones (by about 25%), the relative difference in toughness between pure nt-diamond and nt-diamond composite is consistent in these two methods. The greater toughness of nt-diamond composite is most likely due to the presence of non-3C polytypes. Figure 3g summarizes the toughness and hardness of typical engineering metals and ceramics, indicating an excellent combination of high hardness and toughness of nt-diamond and its composite[2,11,23–28].

To clarify the toughening mechanism at the atomic scale, an in situ fracture test was conducted in the TEM on a specially designed nt-diamond composite sample, as schematically shown in Fig. 4a. During the fracture test, initially a stress concentration region developed near the notch tip, acting as a dislocation emitting source that is evidenced by the extended dislocation with a Burgers vector of 1/2 <110> imaged in situ near the crack tip (Extended Data Fig. 7e, f). With increasing load, a crack initiated from the notch tip and propagated upward, as shown in Fig. 4b. The high-resolution STEM image (Fig. 4c, corresponding to the yellow box in Fig. 4b) shows the fracture surface in 3C nanotwins after the crack passed by. This fracture segment is characterized by atomically sharp {111} cleavage surfaces, corresponding to the straight slip planes in 3C diamond[29]. The crack was transiently arrested at the TB and then deflected into another twin domain, again following {111} planes, leading to a zigzag propagating path (indicated by the blue lines in Fig. 4c) through 3C nanotwins. This is schematically

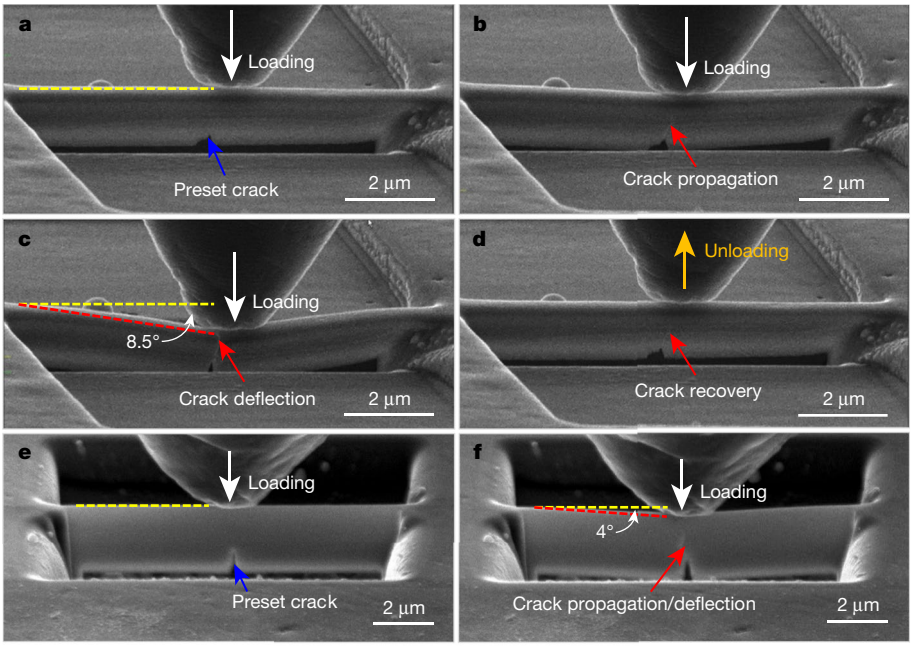

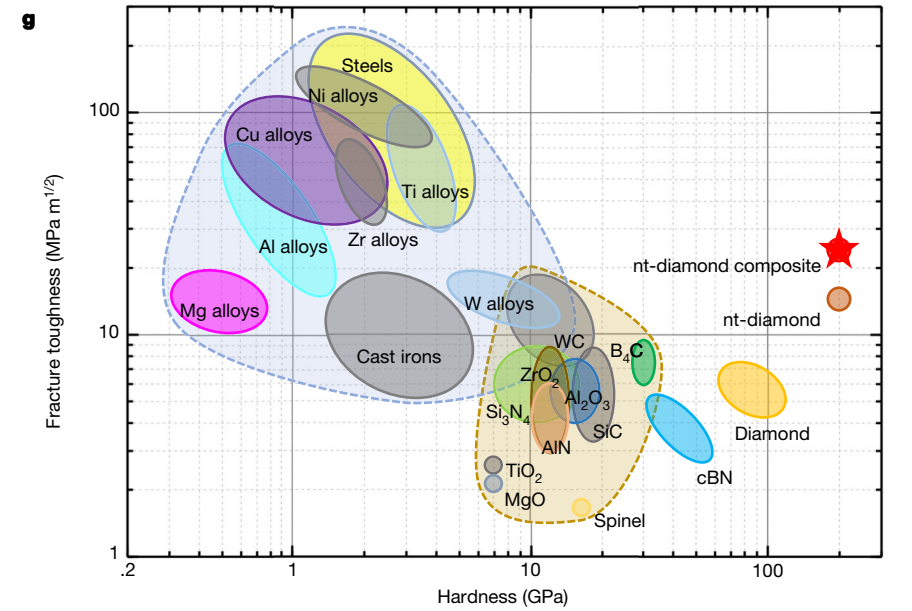

Fig. 3 | Snapshots from in situ bending test and summarized mechanical performance of typical engineering materials. a–**d**, Snapshots of an nt-diamond composite micro-beam during the SENB test. **e**–**f**, Snapshots of a pure nt-diamond micro-beam during the SENB test. Panels **c** and **f** correspond to the time point when the crack reached the top region of the test beams. **g**, Ashby plot of hardness against fracture toughness for nt-diamond composite compared with typical engineering metals and ceramics. cBN, cubic boron nitride.

illustrated in Fig. 4a (pink box), where the nearly straight crack surface deflects from {111} plane to the equivalent $\{111\}_T$ plane in adjacent twin domain after crossing a TB.

In contrast, fractured surfaces in non-3C polytype regions (Fig. 4d, corresponding to the red box in Fig. 4b) show sinuous and wavy boundaries (yellow dashed lines in Fig. 4d) with a tapered fracture edge (green arrows in the schematic diagram of Fig. 4a and in Fig. 4e indicate the direction of decreasing thickness). This is a characteristic of pull-out fracture mode (Extended Data Fig. 7a–d) that is favourable for energy dissipation and toughening. The green box in the lower part of Fig. 4a, which depicts the wavy crack surface at the nanoscale, illustrates the effects of crack propagation by the second mode, due to the presence of non-3C polytype domains that share coherent interfaces with 3C diamond. Unlike 3C diamond, these non-3C polytypes only have one main slip system that is parallel to the interface. When a crack from 3C diamond reaches the interface with non-3C polytypes, the strong coherent interfaces, similar to TBs, deflect the crack. Owing to the variable stacking sequence of carbon bilayers and the absence of straight slip systems in the direction of crack propagation, the crack then deflects continually within non-3C polytype regions (in a path with various atomic-scale steps as indicated by the white dotted line in Fig. 2c), resulting in wavy, sinuous fracture surfaces as shown in Fig. 4d. Closer examination of the fracture surface of non-3C polytype regions reveals a structural transformation into stable 3C diamond (Fig. 4f, an inverse FFT image of the yellow box in Fig. 4e). During crack propagation, very high stress levels develop near the crack tip. First-principles calculations show that transformation from 9R to 3C diamond is preferred under shear along the (001) $[11\bar{2}]$ direction of the 9R lattice, rather than the collapsed layer structure (Extended Data Fig. 8). Such a structural change provides an additional toughening mechanism similar to that occurring in partially stabilized zirconium oxide[8].

During SENB tests, we observed large deflections (about 8.5°, Fig. 3c) in the test beam of nt-diamond composite. Finite element simulations (Extended Data Fig. 9) show that, to achieve such a deflection angle, the test beam must endure an axial strain larger than 10%. The beam deflection in pure nt-diamond is less than half of that in nt-diamond composite (Fig. 3f), indicating additional toughening in the composite. Another peculiarity discovered from the SENB tests is that, after retreating the

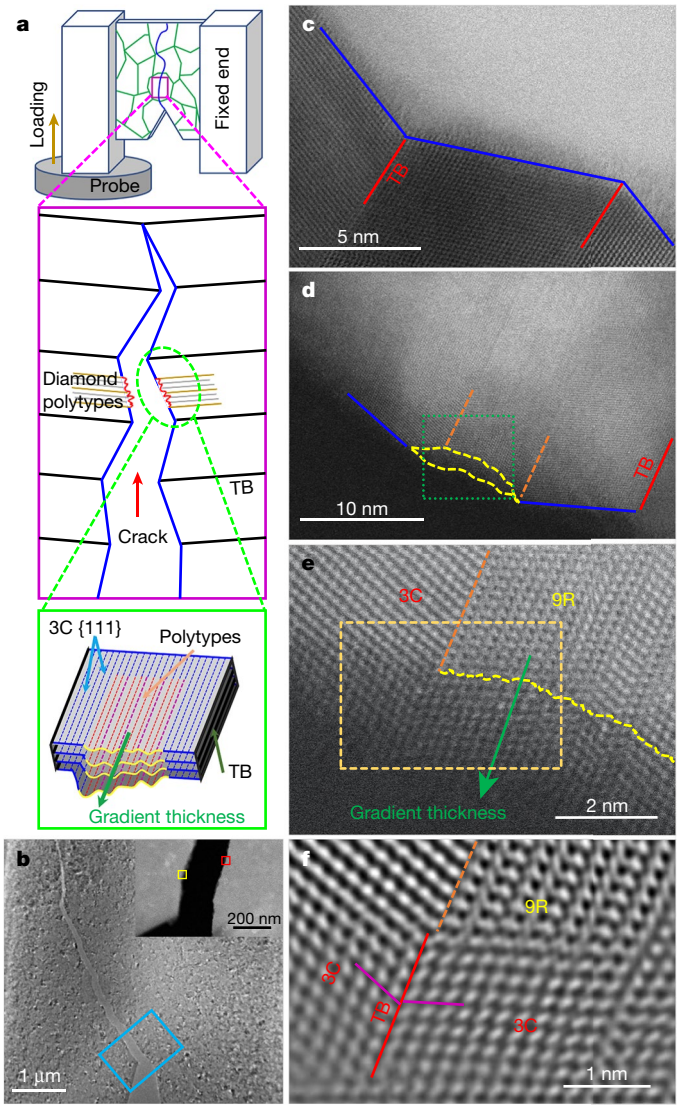

Fig. 4 | In situ bending test of nt-diamond composite in TEM. a, Schematic diagrams of the U-shaped sample used for the in situ bending test in TEM. Enlarged pink box shows crack propagation paths in diamond nanotwins and diamond polytypes (pink box). Enlarged green box illustrates the fracture surface in non-3C diamond polytypes. **b**, TEM image of fractured nt-diamond composite. Inset, STEM image taken from the cyan frame (open space is black). **c**, Annular bright-field image taken from the yellow box in **b**. The crack opening is upper right. **d**, STEM image taken from the red box in **b**. The crack opening (black) is lower left. **e**, Enlarged STEM image corresponding to the green dashed box in **d**. **f**, Inverse FFT image corresponding to the yellow box in **e**, showing that part of the 9R diamond has transformed to 3C diamond along the crack propagation path.

probe (Fig. 3d), the crack in nt-diamond composite healed to a considerable extent, as confirmed by two additional rounds of multi-cycle bending tests on the same beam (Extended Data Fig. 5, Supplementary Videos 1–3). A comparison between the force–displacement curves reveals that, after the yielding point, the test beam was still able to endure load in the second-round test, although its strength was substantially lower than in the first one (Extended Data Fig. 5j,k). This can be attributed to partial self-healing of the crack tip: that is, re-bonding of some dangling carbon bonds on two opposite fractured surfaces near the crack tip after unloading.

The synergetic effects of nanotwins, laminated composite and phase-transformation toughening can effectively disperse energy in nt-diamond composite and lead to enormous enhancement of the fracture toughness. Localized layer-defects with an enlarged interlayer distance (for example, those imaged in Fig. 2c) may also contribute to toughening. This structural architecture strategy could promote the development of superhard materials and engineering ceramics for simultaneously enhanced hardness and toughness, with great potential for cost reduction and lifetime extension, as well as future technical innovation.

Online content

Any methods, additional references, Nature Research reporting summaries, source data, extended data, supplementary information, acknowledgements, peer review information; details of author contributions and competing interests; and statements of data and code availability are available at https://doi.org/10.1038/s41586-020-2361-2.

1. Irifune, T., Kurio, A., Sakamoto, S., Inoue, T. & Sumiya, H. Ultrahard polycrystalline diamond from graphite. *Nature* **421**, 599–600 (2003).
2. Huang, Q. et al. Nanotwinned diamond with unprecedented hardness and stability. *Nature* **510**, 250–253 (2014).
3. Shin, Y. A. et al. Nanotwin-governed toughening mechanism in hierarchically structured biological materials. *Nat. Commun.* **7**, 10772 (2016).
4. Munch, E. et al. Tough, bio-inspired hybrid materials. *Science* **322**, 1516–1520 (2008).
5. Bouville, F. et al. Strong, tough and stiff bioinspired ceramics from brittle constituents. *Nat. Mater.* **13**, 508–514 (2014).
6. Mao, L.-B. et al. Synthetic nacre by predesigned matrix-directed mineralization. *Science* **354**, 107–110 (2016).
7. Zhang, Y. et al. Graphene-based artificial nacre nanocomposites. *Chem. Soc. Rev.* **45**, 2378–2395 (2016).
8. Hannink, R. H. J., Kelly, P. M. & Muddle, B. C. Transformation toughening in zirconia-containing ceramics. *J. Am. Ceram. Soc.* **83**, 461–487 (2000).
9. Li, F. et al. Dual-phase super-strong and elastic ceramic. *ACS Nano* **13**, 4191–4198 (2019).
10. Drory, M. D., Dauskardt, R. H., Kant, A. & Ritchie, R. O. Fracture of synthetic diamond. *J. Appl. Phys.* **78**, 3083–3088 (1995).
11. Ashby, M. F. *Materials Selection in Mechanical Design* 5th edn (Elsevier, 2017).
12. Lu, L., Chen, X., Huang, X. & Lu, K. Revealing the maximum strength in nanotwinned copper. *Science* **323**, 607–610 (2009).
13. Yue, Y., Zhang, Q., Yang, Z., Gong, Q. & Guo, L. Study of the mechanical behavior of radially grown fivefold twinned nanowires on the atomic scale. *Small* **12**, 3503–3509 (2016).
14. Lu, K. Stabilizing nanostructures in metals using grain and twin boundary architectures. *Nat. Rev. Mater.* **1**, 16019 (2016).
15. Wen, B., Zhao, J., Bucknum, M. J., Yao, P. & Li, T. First-principles studies of diamond polytypes. *Diam. Relat. Mater.* **17**, 356–364 (2008).
16. Sennour, M., Lartigue-Korinek, S., Champion, Y. & Hÿtch, M. J. HRTEM study of defects in twin boundaries of ultra-fine grained copper. *Phil. Mag.* **87**, 1465–1486 (2007).
17. Wang, Y. B., Wu, B. & Sui, M. L. Dynamical dislocation emission processes from twin boundaries. *Appl. Phys. Lett.* **93**, 041906 (2008).
18. Németh, P. et al. Lonsdaleite is faulted and twinned cubic diamond and does not exist as a discrete material. *Nat. Commun.* **5**, 5447 (2014).
19. Greshnyakov, V. A., Belenkov, E. A. & Brzhezinskaya, M. M. Theoretical investigation of phase transitions of graphite and cubic 3C diamond into hexagonal 2H diamond under high pressures. *Phys. Status Solidi B* **256**, 1800575 (2019).
20. Kubo, T. et al. An in situ X ray diffraction study of the α–β transformation kinetics of Mg_2SiO_4. *Geophys. Res. Lett.* **25**, 695–698 (1998).
21. Ji, C. et al. Shear-induced phase transition of nanocrystalline hexagonal boron nitride to wurtzitic structure at room temperature and lower pressure. *Proc. Natl Acad. Sci. USA* **109**, 19108–19112 (2012).
22. E1820. *Standard Test Method for Measurement of Fracture Toughness* (American Society for Testing and Materials, 2006).
23. Tian, Y. et al. Ultrahard nanotwinned cubic boron nitride. *Nature* **493**, 385–388 (2013).
24. Tatarko, P. et al. Toughening effect of multi-walled boron nitride nanotubes and their influence on the sintering behaviour of 3Y-TZP zirconia ceramics. *J. Eur. Ceram. Soc.* **34**, 1829–1843 (2014).
25. Xu, F. M., Zhang, Z. J., Shi, X. L., Tan, Y. & Yang, J. M. Effects of adding yttrium nitrate on the mechanical properties of hot-pressed AlN ceramics. *J. Alloys Compd.* **509**, 8688–8691 (2011).
26. Liu, C. et al. Texture, microstructures, and mechanical properties of AlN-based ceramics with Si_3N_4–Y_2O_3 additives. *J. Am. Ceram. Soc.* **100**, 3380–3384 (2017).
27. Ritchie, R. O. The conflicts between strength and toughness. *Nat. Mater.* **10**, 817–822 (2011).
28. Gale, W. F. & Totemeier, T. C. *Smithells Metals Reference Book* 8th edn (Elsevier Butterworth-Heinemann, 2004).
29. Zhang, Y. et al. Direct observation of super-plasticity of beta-SiC nanowires at low temperature. *Adv. Funct. Mater.* **17**, 3435–3440 (2007).

Methods

Sample synthesis

We synthesized nt-diamond composites from onion carbon precursors at 15 GPa and 2,000 °C with the procedure reported earlier[2]. High-pressure high-temperature experiments were performed with a 10-MN double-stage large-volume multi-anvil system by using standard COMPRES 10/5 sample assembly consisting of a 10-mm spinel + MgO octahedron with a Re heater and a $LaCrO_3$ thermal insulator. Temperature was measured with type C thermocouples, and pressure estimated from previously determined calibration curves. The synthesized samples were 1–2 mm in diameter and 0.3–0.5 mm thick.

Sample preparation

To eliminate possible illusion in STEM imaging due to grain overlap, STEM specimens with thickness of about 80 nm were cut by FIB (FEI Scios Dual Beam) and further thinned to 20 nm by low-energy Ar milling (Fischione Model 1040 NanoMill). Before loading into the microscope, the specimens were cleaned with H_2/O_2 plasma (Gatan 695 Plasma cleaner) for 40 s to eliminate possible carbon contamination.

An FEI Helios Nanolab 600i system with an accelerating voltage of 30 kV was used to prepare the TEM foils for microstructure characterization and the micrometre-sized beams for the SENB tests. At the initial stage of the milling process, a current of 790 pA was used to excavate two craters separated by a thin wall. This wall was then either taken out as a thin foil for TEM observations or further machined into a test beam, with its two ends connected to the bulk sample. A tungsten tip was used to extract the foil as shown in Extended Data Fig. 5a. Next, we used lower currents ranging from 80 pA to 7.7 pA to further polish the sample to the desired dimensions. The low currents ensured that irradiation damage was minimized. Examples of the prepared thin foil and the cantilever are shown in Extended Data Fig. 5b and c, respectively.

Structure characterization

STEM measurements were performed by a spherical-aberration-corrected scanning transmission electron microscope (FEI Themis Z), with a monochromator, operating at an accelerating voltage of 300 kV. Bright-field, ADF and HAADF images were obtained by combining 20 frames from the acquired series with drift correction (DCFI in Velox software, Thermo Fisher). The probe convergence angle was set at 25 mrad. The collecting angles of bright-field and ADF were set at 6 mrad and 16–62 mrad, respectively. The collecting angle of HAADF was set at 65–200 mrad to eliminate effects of coherent scattering. The *d*-spacings determined from FFT of HAADF-STEM images of nt-diamond composite are listed in Extended Data Table 1, where theoretically calculated *d*-spacings of diamond polytypes are also listed for comparison[30,31]. Electron energy-loss spectroscopy measurements were performed on a Themis Z equipped with an Enfinium ER/977 spectrometer (Gatan). Precession electron-diffraction measurements were performed with the TEM precession electron-diffraction and nanocrystal analysis system (DigiSTAR P2010/ASTAR, NanoMEGAS).

SENB tests and multiple SENB experiments

SENB tests were conducted in an SEM equipped with an in situ mechanical test instrument (Hysitron PI-85). We prepared micrometre-sized test beams (about 10 μm in length, 0.4 μm in width and 1.3 μm in height), each with a precut notch in the centre point of the underside, to minimize size effect. During the test, a type B diamond nanoindenter with a flat punch (1 μm in size) was pressed against the test beam from the top with a constant displacement rate of 2 nm s^{-1} to initiate cracking from the precut notch. The process of crack propagation was directly observed in the SEM. The applied load and the testing process were recorded in real time by the instrument. In our SENB tests, the crack length was determined based on the simple equivalence between compliance and crack length[5]. The compliance, *C*, was calculated with $C = u/F$, where *u* and *F* are the displacement and applied load at each point after departure of a crack, respectively. The crack length was then recursively calculated with

$$a_n = a_{n-1} + \frac{W - a_{n-1}}{2}\frac{C_n - C_{n-1}}{C_n}, \tag{1}$$

where *W* is the beam height, and *a* and *C* are the crack length and compliance (at steps *n* and $n-1$), respectively[5].

A nonlinear-elastic fracture mechanics approach with the *J*-integral as the driving force for crack initiation and growth was used to evaluate the toughness of our SENB samples[4,5,32]. *J*-integrals were calculated from the recorded applied load–displacement curves[22]. This approach accounts for contributions from both elasticity and plasticity to toughness, and the *J*-integral was calculated as the sum of elastic and plastic contributions, $J = J_{el} + J_{pl}$. The elastic contribution, J_{el}, was calculated from the linear-elastic fracture mechanics[22],

$$J_{el} = \frac{K^2}{E'} = \frac{1-\nu^2}{E}\left[\frac{F_s S}{BW^{3/2}} f\left(\frac{a_n}{W}\right)\right]^2, \tag{2}$$

and

$$f\left(\frac{a_n}{W}\right) = \frac{3\left(\frac{a_n}{W}\right)^{1/2}}{2\left(1+2\frac{a_n}{W}\right)\left(1-\frac{a_n}{W}\right)^{3/2}} \left\{1.99 - \frac{a_n}{W}\left(1-\frac{a_n}{W}\right)\left[2.15 - 3.93\frac{a_n}{W} + 2.7\left(\frac{a_n}{W}\right)^2\right]\right\}, \tag{3}$$

where *E* is the Young's modulus of the sample, *ν* the Poisson's ratio, *B* the specimen width, *W* the sample height, F_s the load value before the *n*th unloading begins and *S* the specimen span. The plastic component, J_{pl}, was calculated as[4,5,22,32]

$$J_{pl} = \frac{2A_{pl}}{Bb}, \tag{4}$$

where A_{pl} is the plastic area under the force–displacement curve for the *n*th loading–unloading cycle, *B* the beam width, and $b = W - a$ the distance from the crack tip to the top edge of the specimen. The calculated *J*-integrals were then converted to equivalent *K* values through the *J*–*K* equivalence (mode I) relationship[4,32], $K_{Jc} = \sqrt{JE'} = \sqrt{JE/(1-\nu^2)}$ (where subscript c means critical), which is the toughness of the sample.

Two additional rounds of SENB bending tests were conducted on the test beam after Fig. 3 was obtained. Extended Data Fig. 5 shows SEM images from the second-round (Extended Data Fig. 5d–f) and third-round (Extended Data Fig. 5g–i) tests. After unloading in the end of the second test, a small bulb-shaped piece of material (marked with the yellow arrow in Extended Data Fig. 5g) was squeezed out from the crack, and torn into halves during the third test (Extended Data Fig. 5h, i). Although the nature of this material remains unknown, the fact that the crack propagated through it suggests that the bulb-like feature bound the left and right sides of the crack after the second test, and thus is direct evidence of the self-healing process. More details can be found in Supplementary Videos 1–3. Extended Data Fig. 5j, k shows force–displacement curves of the first-round and second-round SENB tests. Toughness values calculated from these two tests are 26.6 MPa $m^{1/2}$ and 24.4 MPa $m^{1/2}$, respectively.

Vickers indentation measurements

A microhardness tester (KB 5 BVZ) was used to measure hardness and fracture toughness with a diamond Vickers indenter. The Vickers hardness was determined as $H_V = 1{,}854.4F/L^2$, where *F* (in N) is the applied load and *L* (in μm) is the average diagonal of the Vickers indentation; the indentation fracture toughness was calculated as $0.016(E/H_V)^{0.5}F/C^{1.5}$, where *C* is the average length of the radial cracks measured from the indent centre and *E* is the Young's modulus of diamond as 1,100 GPa.

In situ fracture test in the TEM

A test piece with a dog-bone-shaped cross-section when viewed edge-on was prepared by FIB, consisting of a thin (approximately 70 nm) sheet and two thicker columns (Fig. 4a, Extended Data Fig. 7a). A small notch was precut at the bottom of the thin sheet. For the in situ fracture test, one columnar end was fixed to a special TEM semi-ring mounted on a Nanofactory TEM holder and the other end was pushed by a flat tungsten probe. The in situ fracture test was conducted in a JEOL 2100F TEM, and the crack propagation was monitored in real time. After the test, the special TEM semi-ring was transferred into a JEM ARM 200F to do further structure characterization.

Transformation mechanism from 9R to 3C diamond

The stress–strain curves[33,34] were calculated using the VASP code[35] based on the local density approximation with the functional of Ceperley and Alder as parametrized by Perdew and Zunger[36,37]. The plane-wave cut-off energy of 750 eV and uniform Γ-centred k-point grids with a resolution of $2\pi \times 0.03 Å^{-1}$ were used. To compare the easy slip (or cleavage) plane of 9R and 3C diamonds conveniently, a 12-atom unit cell of 9R diamond, defined on the basis vectors of the six-atom rhombohedral primitive cell with transformation matrix $\begin{pmatrix} 1 & 1 & -2 \\ -1 & 1 & 0 \\ 0 & 0 & 1 \end{pmatrix}$ (Extended Data Fig. 8a, where a 12-atom unit cell of 3C diamond showing different stacking sequence of carbon bilayers is also plotted), was constructed to explore shear-induced phase transformations and energy barriers. For structural relaxation, the lattice vector was incrementally deformed along the direction of applied shear with a strain step of 0.005 (ε_{zx}; see the coordinate system and red/blue arrows in Extended Data Fig. 8a). The other five independent components of the strain tensor and all the atoms were completely relaxed until the convergence criteria for the total energy (10^{-7} eV) and force (0.02 eV $Å^{-1}$) were satisfied.

Finite element simulations of SENB tests

Finite element simulations were performed to evaluate the stress state of the notched test beams. The results (Extended Data Fig. 9b) show that strains larger than 10% are required on the top side of the beam above the notch to achieve the observed deflection shown in Fig. 3c. Stress states in conventional SENB tests (with hinged ends, Extended Data Fig. 9c) and the SENB tests in our work (with fixed ends, Extended Data Fig. 9d) are compared. The stress level is higher in our SENB tests than in conventional SENB tests with the same deflection depth. Furthermore, in our configuration, stresses are more concentrated near the centre of the beam. Both factors cause crack to propagate more easily than in the conventional SENB tests under the same load. Therefore, toughness values calculated in our work, which were based on the formulation for the conventional SENB test configuration, are underestimated.

Data availability

The data that support the findings of this study are available from the corresponding authors on reasonable request.

30. Ownby, P. D., Yang, X. & Liu, J. Calculated X-ray diffraction data for diamond polytypes. *J. Am. Ceram. Soc.* **75**, 1876–1883 (1992).
31. Xue, X. Y., Zhang, R. Q. & Zhang, X. H. Structural and electronic properties of 9R diamond polytype. *Solid State Commun.* **136**, 41–44 (2005).
32. Koester, K. J., Ager, J. W. III & Ritchie, R. O. The true toughness of human cortical bone measured with realistically short cracks. *Nat. Mater.* **7**, 672–677 (2008).
33. Roundy, D. & Cohen, M. L. Ideal strength of diamond, Si, and Ge. *Phys. Rev. B* **64**, 212103 (2001).
34. Pan, Z., Sun, H., Zhang, Y. & Chen, C. Harder than diamond: superior indentation strength of wurtzite BN and lonsdaleite. *Phys. Rev. Lett.* **102**, 055503 (2009).
35. Kresse, G. & Furthmüller, J. Efficient iterative schemes for ab initio total-energy calculations using a plane-wave basis set. *Phys. Rev. B* **54**, 11169–11186 (1996).
36. Ceperley, D. M. & Alder, B. J. Ground state of the electron gas by a stochastic method. *Phys. Rev. Lett.* **45**, 566–569 (1980).
37. Perdew, J. P. & Zunger, A. Self-interaction correction to density-functional approximations for many-electron systems. *Phys. Rev. B* **23**, 5048–5079 (1981).

Acknowledgements This work was supported by the National Key R&D Program of China (2018YFA0703400 and 2018YFA0305900), the National Natural Science Foundation of China (51922017, 51525205, 51772011, 51672239, 51572235, 51741201, 51772260, 51972009, 51532001, 11674176 and 11874224), US National Science Foundation (EAR-1661489 and EAR-1361276) and the Fundamental Research Funds for Central Universities (YWF-19-BJ-J-94). We thank M. Veron at Grenoble Institute of Technology for the precession electron diffraction measurement.

Author contributions Y.T., Y.Y., B.X., X.-F.Z. and L.G. proposed and supervised the project; Y.G., Z.L., P.Y., X.L. and D.Y. synthesized the sample; Y.Y., W.H., B.X., B.G., Z.W., B.W. and X.-F.Z. performed the TEM characterization; Y.Y., J.W., X.Z. and Q.Z. performed the in situ bending experiments; Y.G., P.Y. and B.X. performed the Vickers indentation measurements; X.-F.Z. performed the first-principles calculations; Z.Y. performed the finite element simulations; Y.Y., Y.T., B.X., Y.W., X.-F.Z. and L.G. analysed data and wrote the manuscript. All authors participated in discussions of the research.

Competing interests The authors declare no competing interests.

Additional information

Supplementary information is available for this paper at https://doi.org/10.1038/s41586-020-2361-2.

Correspondence and requests for materials should be addressed to X.-F.Z., L.G. or Y.T.

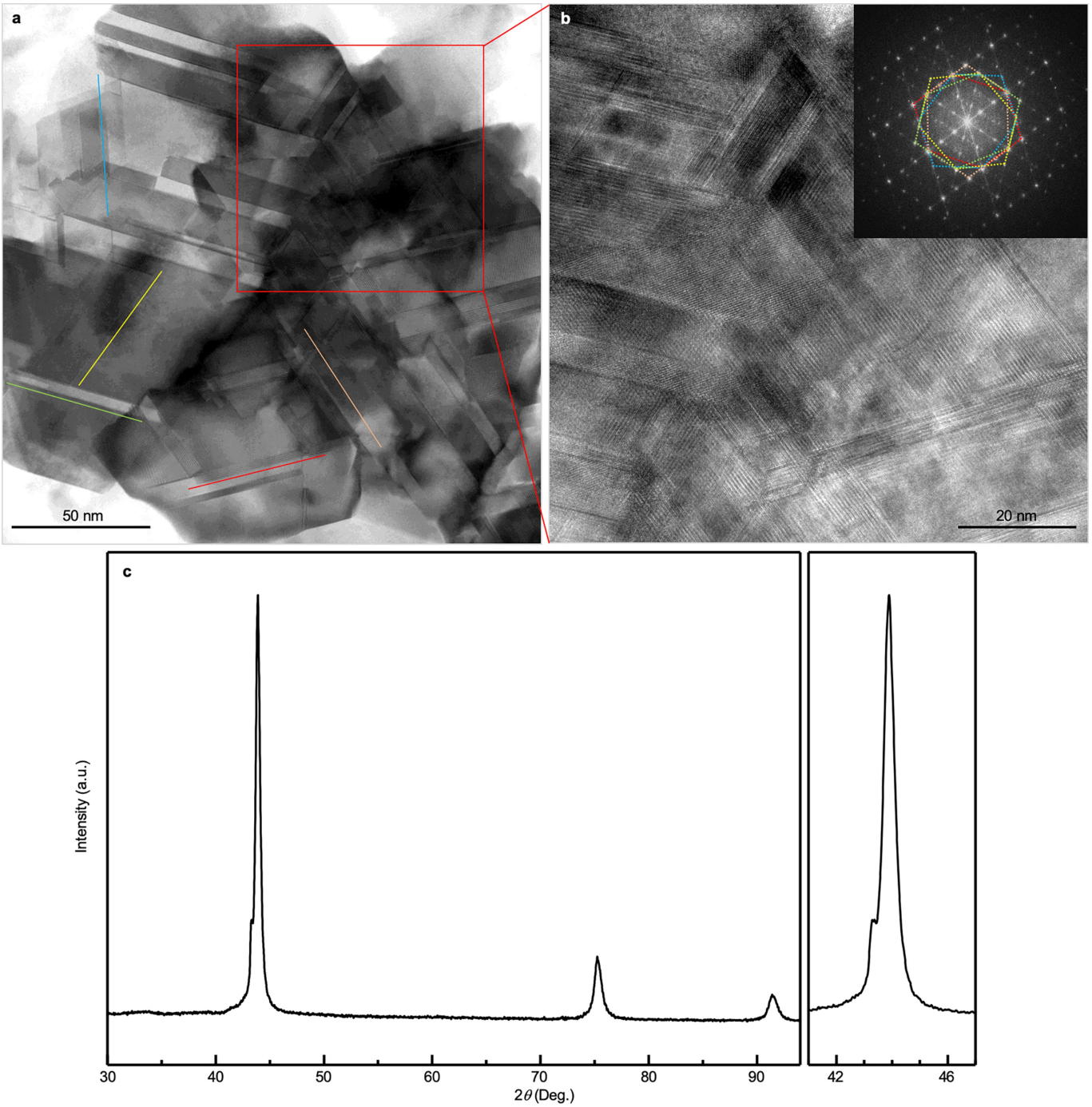

Extended Data Fig. 1 | Microstructure and X-ray diffraction patterns of nt-diamond composite synthesized at 15 GPa and 2,000 °C. **a**, Low-magnification bright-field STEM image showing interlocked grains composed of nanotwins. Coloured lines indicate five different TB orientations. **b**, HRTEM image from the red-boxed region in **a**, showing interwoven nanotwins with embedded secondary phases. Inset shows the corresponding FFT pattern. In addition to the fivefold patterns from the multi-directional 3C diamond twins in the interlocked grains, extra diffraction spots from coherent non-3C diamond polytypes are clearly recognized. **c**, X-ray diffraction characterization. A shoulder is clearly observed at the lower-angle side of 3C diamond (111) peak near 44° (left panel of **c**), an indicator of polytype existence.

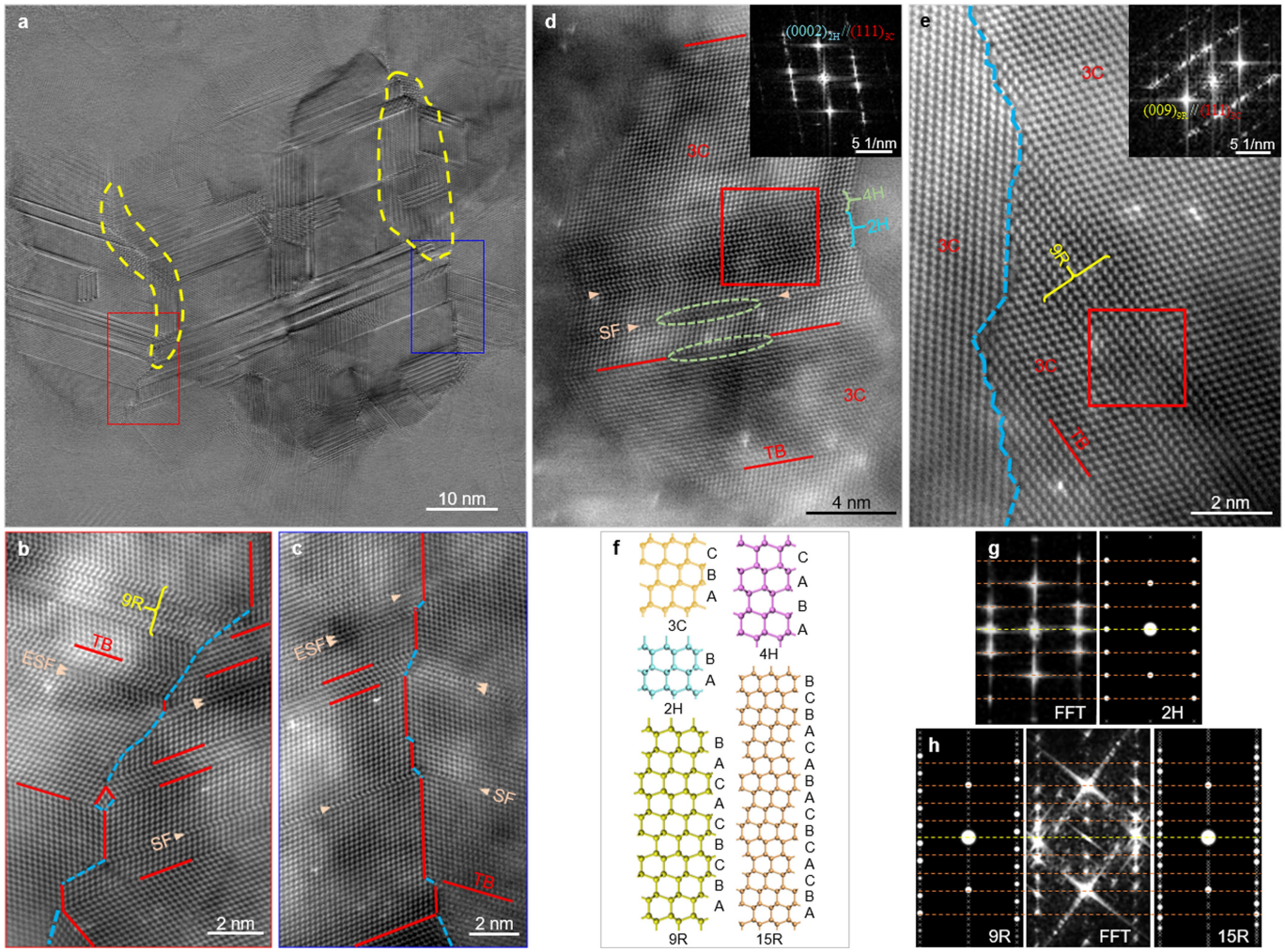

Extended Data Fig. 2 | Hierarchical microstructure of nt-diamond composite. a, Bright-field STEM image showing three interlocked nanograins with boundaries appearing diffuse or segmented by intersecting twin boundaries. The Moiré fringes (enclosed with yellow-dashed lines) indicate three-dimensional interpenetrating grain boundaries, which lock neighbouring grains and cause grain overlapping near the boundaries. **b**, **c**, HAADF-STEM images corresponding to the red and blue boxes in **a**, respectively, displaying segmented boundaries with {111} TBs (red lines) and other boundaries (cyan lines). SFs (single arrowheads) and ESFs (double arrowheads) are also marked. A 9R polytype region is also clearly recognizable in **b**. **d**, HAADF-STEM image of 3C nanotwins with coherently embedded 2H and 4H polytypes. Inset, FFT pattern corresponding to the red-boxed area, showing the symmetry of 2H and 4H polytypes. TBs and SFs are marked with red lines and arrowheads, respectively. Layer defects are marked with green ovals. Along the long axes of the ovals, the TB and stacking fault climb by one bilayer. **e**, HAADF-STEM image of a 9R polytype region coherently embedded in 3C diamond. The cyan dashed line indicates the grain boundary. Inset, FFT pattern corresponding to the red-boxed area, showing a tripling of $(111)_{3C}$ periodicity. **f**, Stacking sequences of 3C, 2H, 4H, 9R and 15R polytypes. **g**, Simulated electron diffraction pattern of 2H polytype (right) compared with experimental FFT pattern (left; inset of Fig. 2b). **h**, Simulated electron diffraction patterns of 9R (left) and 15R (right) polytypes compared with experimental FFT pattern (middle; inset of Fig. 2c).

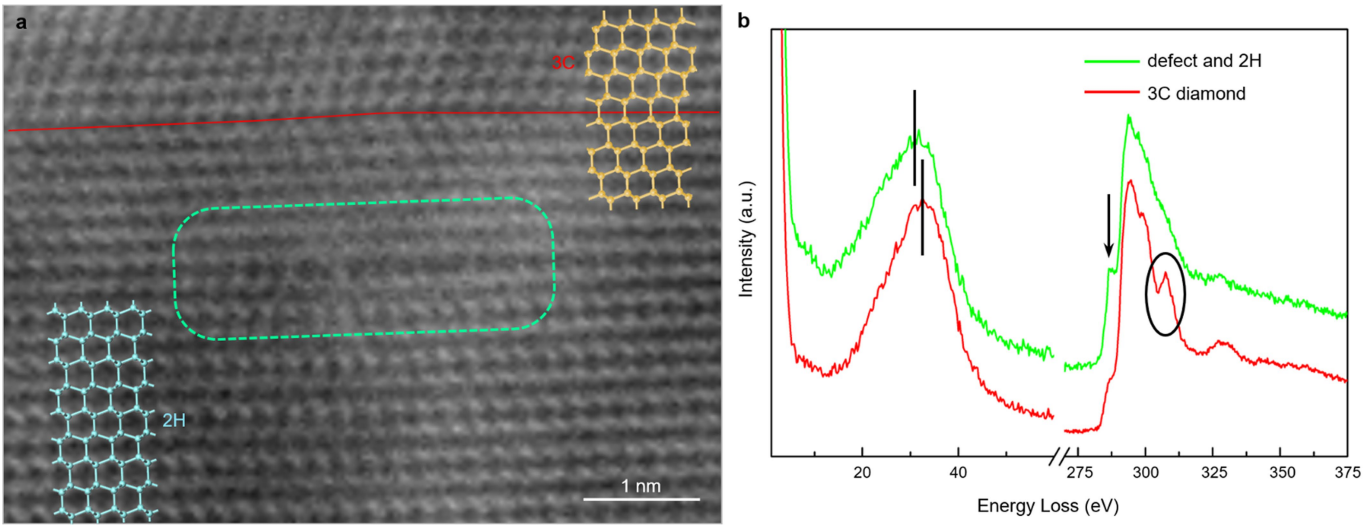

Extended Data Fig. 3 | Details of a localized layer defect in nt-diamond composite. a, A high-resolution HAADF-STEM image shows a localized layer defect between 3C and 2H domains (green-dashed frame). The carbon bilayers and the TB (red line) are obviously bent because of the bulge produced by the defect. **b**, Electron energy-loss spectra from the defective region (green) and 3C diamond region (red). Note that the region with the layer defect exhibits a peak near 286 eV (black arrow), suggesting sp^2 bonds in the layer defect and consistent with the enlarged interlayer distance. The 3C region, on the other hand, exhibits peaks typical of diamond.

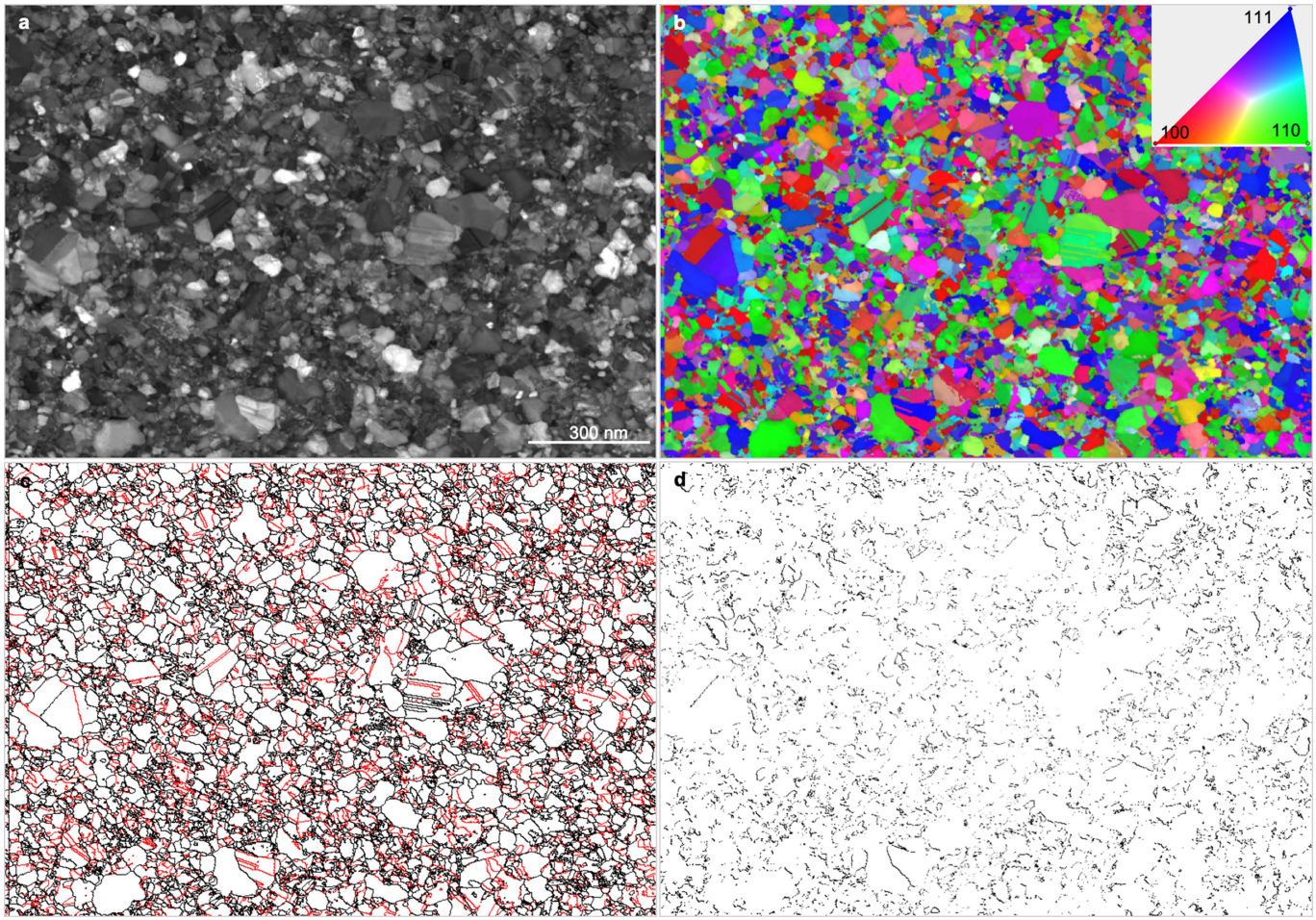

Extended Data Fig. 4 | Crystallographic characterization of nt-diamond composite with precession electron diffraction. a, Virtual bright-field image. **b**, Crystallographic orientation map corresponding to **a**. Inset, the chromatic code of the cubic inverse pole figure. **c**, Grain and twin boundaries, among which the Σ3 boundaries are coloured in red. **d**, Remaining grain boundaries after removing Σ3 and Σ9 low-energy boundaries, indicating a substantial grain interlocking. The average grain size in nt-diamond composite is 22 nm as determined by precession electron diffraction.

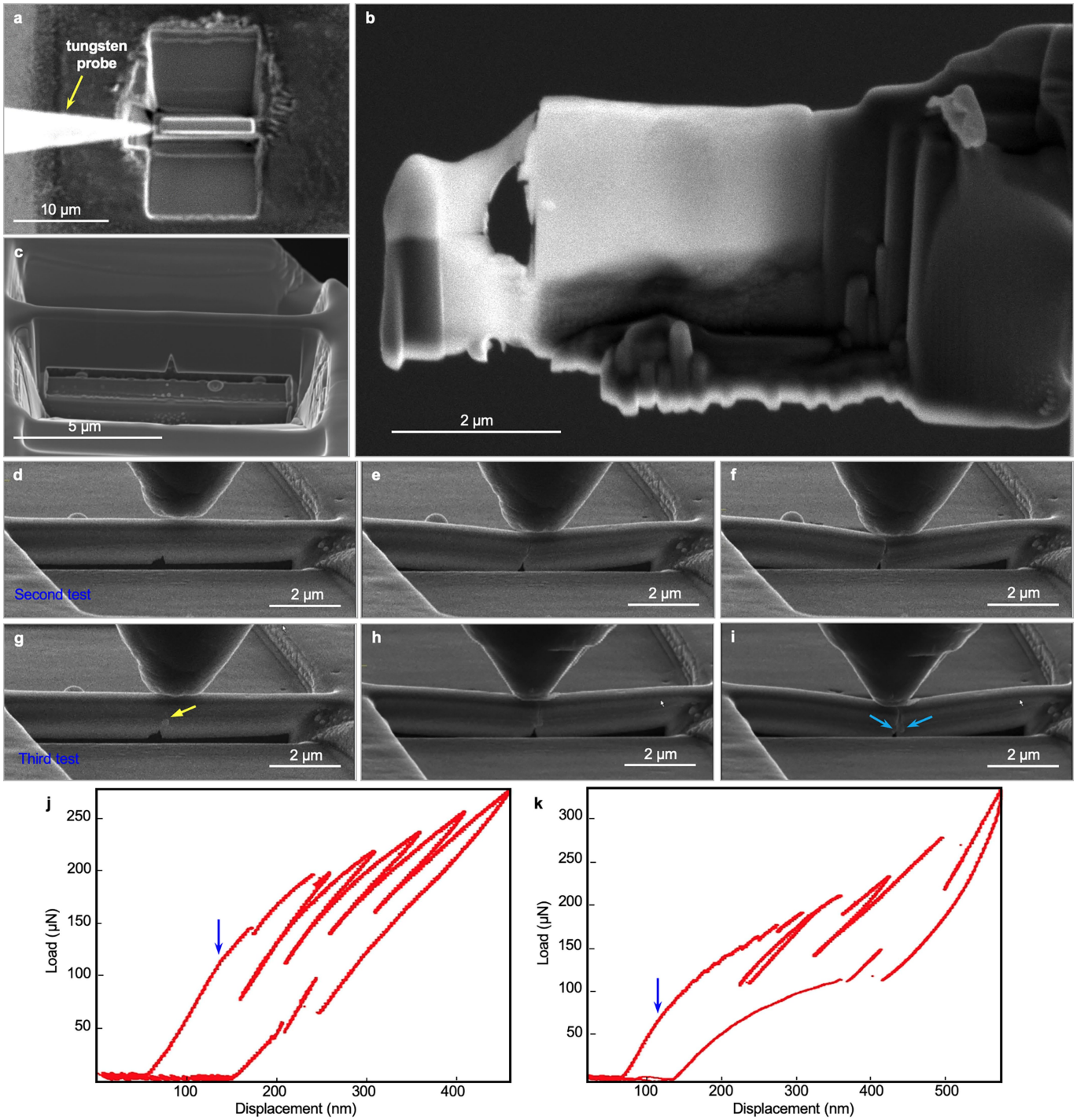

Extended Data Fig. 5 | SENB sample preparation and time-sequential SENB bending tests. Sample preparation was with FEI (Helios Nanolab 600i). Time-sequential SENB bending tests were carried out on sample 3 after the first test shown in Fig. 3. **a**, SEM image of the sample after excavating craters, with a thin wall in between. **b**, A thin wall taken out to prepare TEM foil. **c**, A micro-beam shaped from the thin wall described in **a**. Note the precut notch on the underside of the micro-beam. **d**–**f**, SEM images from the second-round multi-cycle bending test. **g**–**i**, SEM images from the third-round test. **j**, **k**, Force–displacement curves of the first- and second-round SENB tests. Blue arrows indicate yielding points.

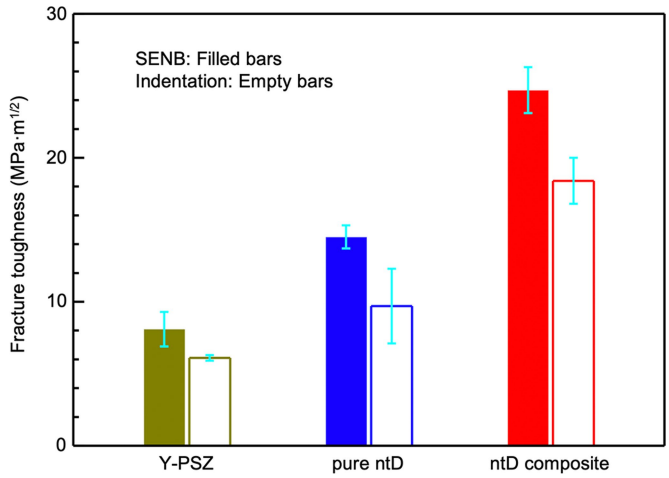

Extended Data Fig. 6 | Comparison of fracture toughness values from SENB and indentation measurements for Y-PSZ, pure nt-diamond and nt-diamond composite. SENB, filled bars; indentation, empty bars. The loads for indentation fracture toughness measurement were 49 N for Y-PSZ, and 19.6 N for pure nt-diamond and nt-diamond composite. Error bars indicate 1 s.d. (n = 5 for Y-PSZ and nt-diamond composite, n = 3 and 5 for indentation and SENB measurements of pure nt-diamond, respectively). ntD, nt-diamond.

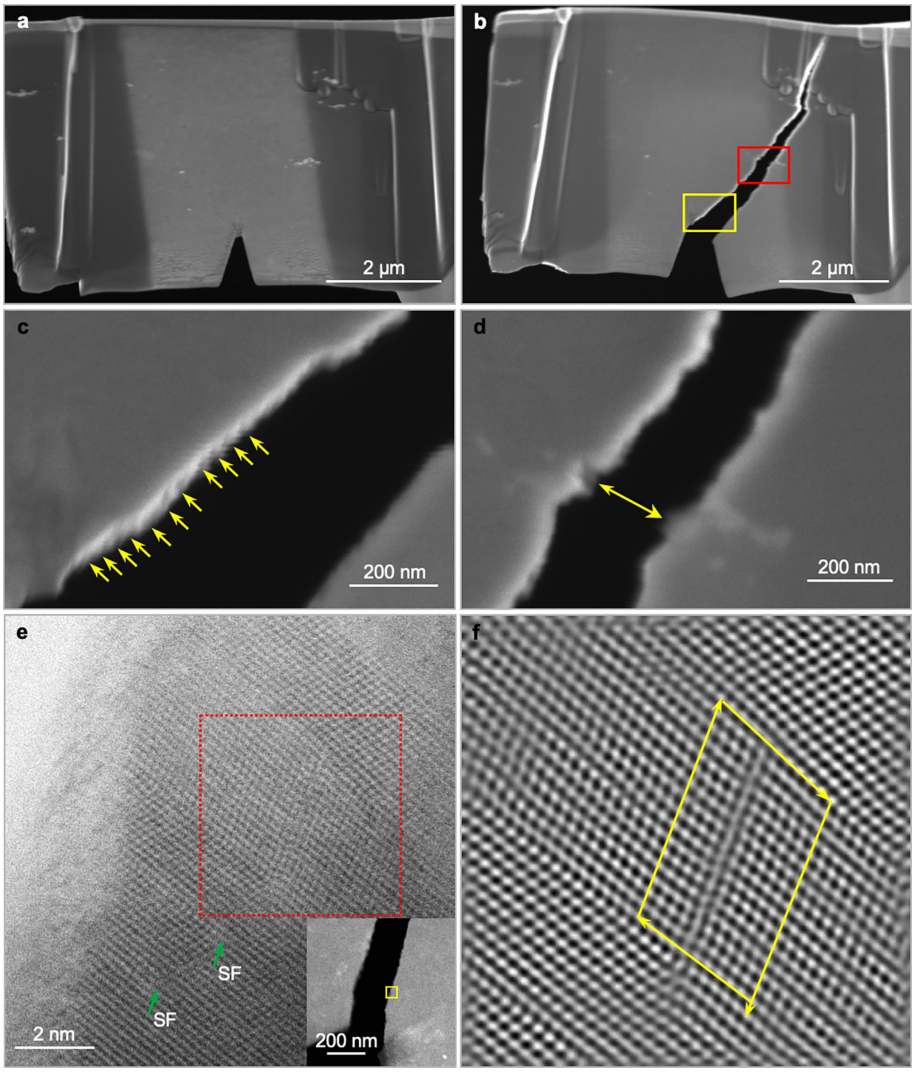

Extended Data Fig. 7 | An nt-diamond composite before and after in situ fracture test in TEM. a–**d**, SEM observation of the test piece. **a**, Before the fracture test. **b**, After the fracture test. **c**, **d**, Enlarged SEM images corresponding to the yellow and red boxes in **b**, respectively. Arrows in **c** highlight the sinuous crack propagation path in non-3C polytypes. Double-headed arrow in **d** indicates a pull-out fracture in nt-diamond composite. Such pull-out fractures are common in composite materials with enhanced toughness. **e**, **f**, Plastic deformation near the crack tip from in situ TEM observation. **e**, HRTEM image of nt-diamond composite taken near the crack tip (corresponding to the small yellow box in the inset) where stacking faults (green arrows) can be identified. **f**, Inverse FFT image corresponding to red box in **e**. An extended dislocation with a Burger's vector of 1/2 <110> is clearly shown by the Burger's circuit (yellow).

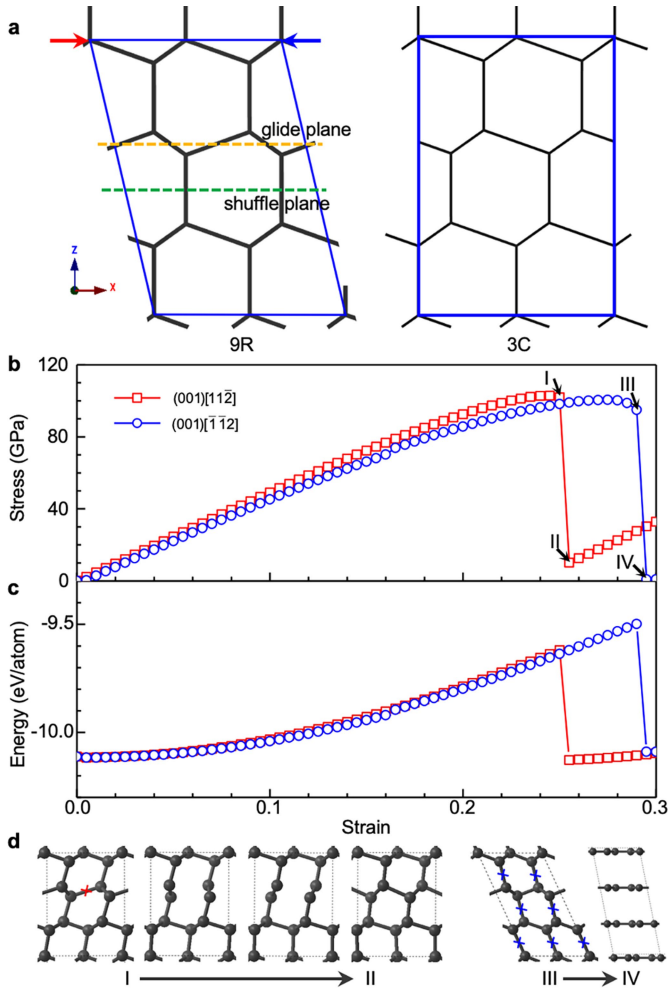

Extended Data Fig. 8 | Structural transformation from 9R diamond to 3C diamond. a, Projection view of 9R and 3C diamonds with redefined unit cells. The yellow and green dashed lines represent the glide and shuffle planes, respectively. **b**, Stress–strain curves of 9R diamond sheared along (001)[11$\bar{2}$] and (001)[$\bar{1}\bar{1}$2] directions, corresponding to the red and blue arrows in **a**, respectively. The peaks of shear stress in these two directions are 103 GPa and 101 GPa, indicating no distinct easy or hard directions. **c**, Energy–strain curves of 9R diamond along (001)[11$\bar{2}$] and (001)[$\bar{1}\bar{1}$2] directions. **d**, Structural snapshots from I to II (sheared along (001)[11$\bar{2}$] and from III to IV (sheared along (001)[$\bar{1}\bar{1}$2]). Points I–IV are marked in **b**. The calculated energy–strain curves indicate that 9R to 3C transformation with a smaller energy barrier is preferred, rather than the collapsed layer structure. Under shear along (001)[11$\bar{2}$], C–C bonds across shuffle planes are tilted towards (001)[11$\bar{2}$], with one-ninth of bonds across glide planes broken beyond critical strain (two bonds per unit cell, marked with red cross in **d**). In comparison, all bonds across shuffle planes (six bonds per unit cell, marked with blue crosses in **d**) are broken under shear along (001)[$\bar{1}\bar{1}$2].

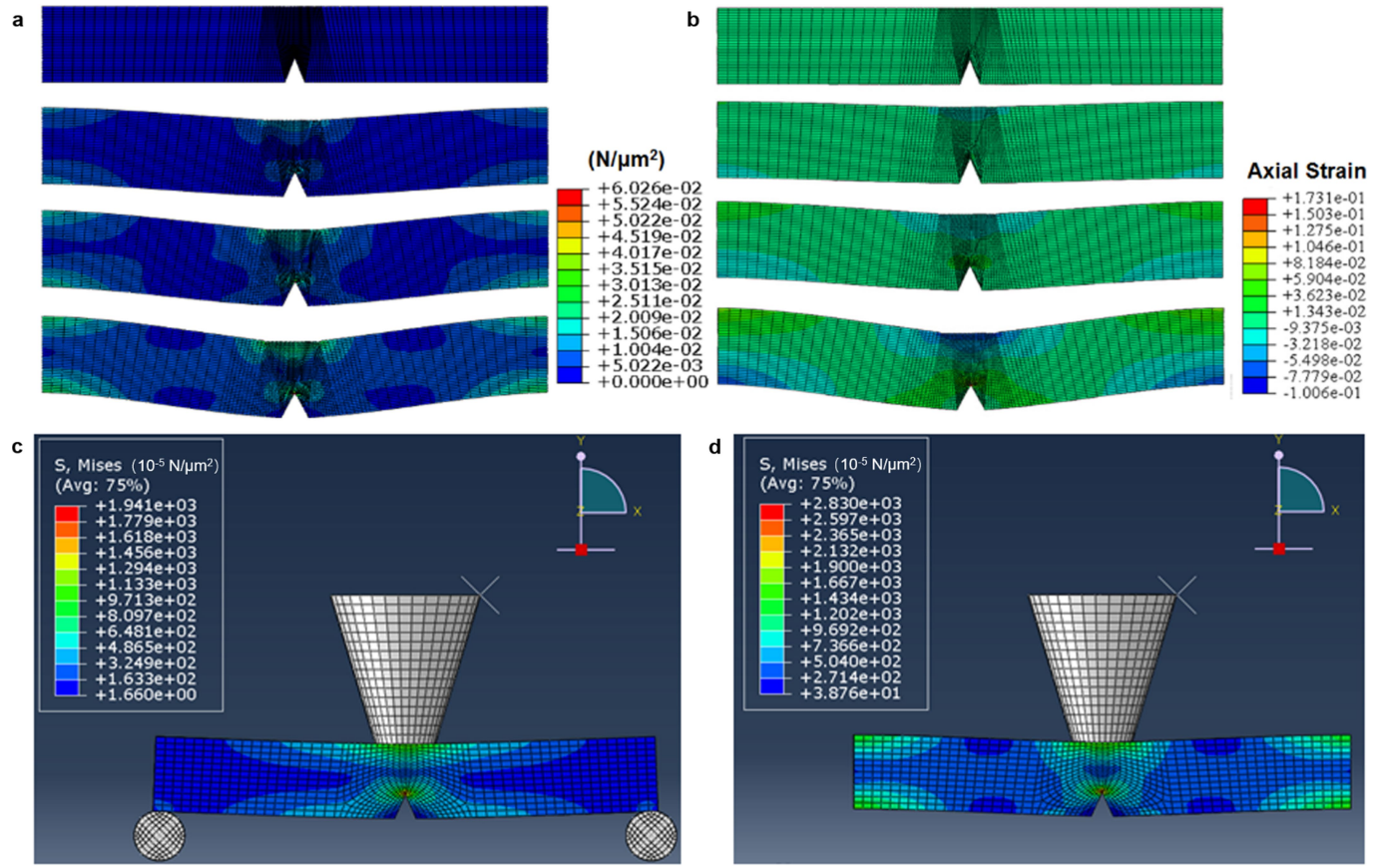

Extended Data Fig. 9 | Finite element simulation results of SENB tests. **a**, von Mises stress distribution in the bending test with increasing load. **b**, Axial strain distribution in the cantilever corresponding to **a**. **c**, The stress distribution in conventional SENB test with hinged ends. **d**, The stress distribution in our SENB test with fixed ends.

Extended Data Table 1 | *d*-spacings

3C	2H	4H	9R	15R	d_{obs}
	0.21842 / (0 1 0)	0.21842 / (0 1 0)		0.21788 / (0 1 $\bar{1}$)	0.219
			0.21647 / (0 1 $\bar{1}$)	0.21627 / (0 1 2)	0.215
		0.21112 / (0 1 1)	0.21226 / (0 1 2)	0.21018 / (0 1 $\bar{4}$)	0.213
			0.20812 / (0 0 9)		0.208
0.2059 / (1 1 1)	0.20593 / (0 0 2)	0.20593 / (0 0 4)		0.20593 / (0 0 15)	0.206
			0.19758 / (0 1 $\bar{4}$)	0.19575 / (0 1 $\bar{7}$)	0.198
	0.19296 / (0 1 1)	0.19296 / (0 1 2)		0.19011 / (0 1 8)	0.191
			0.18837 / (0 1 5)		0.189
		0.17093 / (0 1 3)		0.17161 / (0 0 18)	0.173
			0.16898 / (0 1 $\bar{7}$)		0.167
				0.16080 / (0 1 $\bar{13}$)	0.161
			0.15952 / (0 1 8)	0.15523 / (0 1 14)	0.159
	0.14984 / (0 1 2)	0.14984 / (0 1 4)		0.14709 / (0 0 21)	0.147
			0.14205 / (0 1 $\bar{10}$)	0.13969 / (0 1 17)	0.140
		0.13729 / (0 0 6)	0.13418 / (0 1 11)		0.135
		0.13153 / (0 1 5)		0.13042 / (0 1 $\bar{19}$)	0.132
				0.12871 / (0 0 24)	0.129
0.1261 / (2 2 0)	0.12611 / (1 1 0)	0.12611 / (1 1 0)	0.12582 / (1 1 0)	0.12611 / (0 1 20)	0.126
		0.12058 / (1 1 2)	0.12019 / (0 1 $\bar{13}$)		0.121
	0.11623 / (0 1 3)	0.11623 / (0 1 6)		0.11811 / (0 1 $\bar{22}$)	0.116
			0.11402 / (0 1 14)	0.11441 / (0 1 23)	0.113
	0.10921 / (0 2 0)	0.10921 / (0 2 0)	0.10878 / (0 2 1)	0.10914 / (0 2 1)	0.108
		0.10826 / (0 2 1)	0.10823 / (0 2 $\bar{2}$)	0.10894 / (0 2 $\bar{2}$)	
0.1075 / (3 1 1)	0.10754 / (1 1 2)	0.10754 / (1 1 4)	0.10767 / (1 1 9)	0.10754 / (0 1 $\bar{25}$)	0.106

The *d*-spacings determined from FFT of HAADF-STEM images of nt-diamond composite sample (15 GPa and 2,000 °C) are compared with theoretical values of selected diamond polytypes[30,31].

Extended Data Table 2 | Toughness of nt-diamond composite, pure nt-diamond and Y-PSZ samples from SENB tests

Sample	Sample No.		Fracture toughness ($MPa \cdot m^{1/2}$)
nt-diamond composite	1		23.9
	2		22.5
	3	1st test	26.6
		2nd test	24.4
	4		24.7
	5		25.9
pure nt-diamond	1		15.7
	2		14.5
	3		13.8
	4		14.3
	5		14.5
Y-PSZ	1		8.9
	2		7.7
	3		6.3
	4		9.5
	5		8.0